ELSEVIER

Journal of Hazardous Materials 55 (1997) 23–37

JOURNAL OF HAZARDOUS MATERIALS

In-situ monitoring of electrochemical transport processes in Hanford Grout Vault Soil

Daniel T. Schwartz [a,*], Mark F. Buehler [b,1], Derek X. Christiansen [a,2], E. James Davis [a]

[a] *Department of Chemical Engineering, Box 351750, University of Washington, Seattle, WA 98195-1750 USA*
[b] *Chemical Process Development Section, Pacific Northwest Laboratory, Battelle Boulevard, Richland, WA 99352 USA*

Abstract

Real-time spatially-resolved radiotracer and soil conductivity measurements were used to assess the fate of contaminants and the interaction of electrolysis products with Grout Vault Soil from the Department of Energy's Hanford site in Richland, Washington. Radiotracer techniques allowed the extent that a radioactive species was remediated to be unambiguously determined in the laboratory, and the method also provided insight into the immobilization of Cs^+ by adsorption to the soil. Conductivity measurements provided a window into the changing state of the porous medium and the propagation of electrochemically-generated species that were introduced by water electrolysis at each active electrode. Measurements of the velocity of conductivity fronts generated by water electrolysis were combined with detailed geochemical and geophysical data about the soil to evaluate plausible soil chemistries in the system. Based on ion transport rates, it was shown that the alkaline nature of the soil buffered protons generated at the anode and hydroxide anions generated at the cathode titrated surface groups in the soil. © 1997 Elsevier Science B.V.

Keywords: Radiotracer techniques; Water electrolysis; Soil remediation

1. Introduction

In-situ soil remediation processes are normally thought to offer potential cost savings over more traditional dig and treat or pump and treat methods of clean-up. For any in-situ remediation process —including electrochemical techniques — the site must first

* Corresponding author.
[1] Current address: Intel Corporation, D1-50, Hillsboro, OR 97124, USA.
[2] Current address: Fujitsu Microelectronics, Gresham, OR 97030, USA.

PII S0304-3894(97)00015-0

be characterized thoroughly with respect to the extent of the contamination plume and the geochemical and geophysical properties of the contaminated soil. Next, the remediation process must be initiated and monitored to ensure optimal system performance. Finally, a post-remediation site characterization must be performed to verify the efficacy of the process and identify the fate of any remaining contaminants or by-products of the remediation process.

To effectively remediate a site and realize some of the potential costs savings of in-situ techniques, it is desirable to inexpensively monitor and optimize the process in real-time and with spatial resolution. In electrochemical remediation processes, the normal method for real-time process monitoring is to measure the composition of the effluent flowing out of the cathode wells [1,2]. From this measurement the overall remediation efficiency can be determined, provided the contaminant is accurately quantified at the start. However, monitoring the effluent stream does not provide any information about the fate or location of the residual contamination. To obtain spatially-resolved data, sampling wells are usually drilled throughout the site [3]. Samples are then occasionally drawn from the wells and analyzed to estimate the state of remediation. Well drilling and ex-situ sample analysis is neither inexpensive nor a real-time measurement.

Surprisingly, real-time spatially-resolved monitoring is also rarely used in laboratory-scale electrochemical remediation experiments. Rather, it is most common to monitor the cathode effluent in real-time, and then do a post-remediation analysis of the spatial profile of contaminants and electrolysis products [4–12]. Real-time spatially-resolved monitoring is reported in selected instances. For example, pH indicators have been mixed into soil to quantitatively identify the location (and real-time motion) of electrolysis-generated pH fronts as they propagate through the soil [13,14]. There are few cases where real-time spatially-resolved monitoring has gone much beyond this example. In this paper we describe the implementation and effectiveness of real-time spatially-resolved radiotracer and conductivity measurements for understanding transport and chemical processes occurring within porous media during the passage of current. The two techniques we present are complementary, in that, radiotracer methods provide a species-specific view of transport rates in the soil and conductivity measurements probe the overall ionic character of the pore fluids as well as ionic interactions with the charged soil particles.

2. Experimental apparatus and procedure

2.1. Soil characteristics

All of the experiments reported here employed nonradioactive soil from the Department of Energy's Hanford site 200 East Grout Vault. Before any experiments were performed, the soil was sieved using a U.S. mesh size 10 to eliminate large rocks. Comprehensive measurements of the physical and chemical properties of Grout Vault Soil (GVS) have been reported elsewhere [15]. Summarized below are reported values

Table 1
Bulk mineralogy of Grout Vault Soil (Wt.% is shown below each species)[a]

Quartz	Plagioclase	Smectite	Mica	Hornblende	a-Oxides	$CaCO_3$	Kaolinite	Vermiculite
46.1	41.5	5.0	3.1	1.8	1.0	0.8	0.3	0.2

[a]Adapted from reference [15].

for important geophysical and geochemical properties of GVS that influence electrochemical transport processes; all values come from reference [15] unless noted otherwise.

GVS is characterized as sand since $\approx 97\%$ (w/o) of the soil particles have diameters (D_p) that fall in the range $2 \leq D_p \leq 50$ μm. The bulk mineralogy of the GVS is summarized in Table 1. The low crystallinity amorphous oxides (a-Oxides) are predominantly hydrated Al_2O_3, SiO_2, Fe_2O_3 and MnO_2, and the clay fractions of the soil ($D_p < 2$ μm) are predominantly smectite. The average density of the soil particles is 2.82 g/cm^3, the porosity of the soil is approximately 36%, and the hydraulic conductivity (at saturation) is $7.3 \pm 0.9 \times 10^{-2}$ cm/s. The overall cation exchange capacity for GVS is 7.8 ± 0.5 meq/100 g dry soil. When the GVS is saturated with distilled water and then allowed to equilibrate, the saturation extract is found to be alkaline with a pH of 8.07. Chemical analysis of the saturation extract shows that Na^+ is the predominant cation with a concentration of 25.00 mg Na^+ per liter saturation extract (equivalent to 7.42 μg Na^+ per g soil or ≈ 1 meq/liter). Shown in Table 2 is the saturation extract composition for species with concentrations ≥ 0.05 meq/l. The total cation concentration found in the saturation extract was 2.46 meq/l and the total anion concentration was 3.54 meq/l; these totals indicate that the analysis was only 'semi-quantitative' since saturation extracts should satisfy electroneutrality. The apparent zeta potential for GVS falls in the ranges -2 to -10 mV [16]. Thus, GVS has a negative surface charge (q_s), as indicated by the negative zeta potential of the soil.

All of the experiments used GVS that was saturated with either deionized water or a weak electrolyte; saturated GVS contained approximately 16% moisture by weight.

2.2. Radiotracer measurements

A schematic of the stainless steel electrodes, Plexiglas cell, and scintillation detector system is shown in Fig. 1. GVS was saturated with deionized water, mixed thoroughly, and then placed between the rectangular 15.24 cm wide by 5.08 cm high electrodes. The electrode separation was set at 22.86 cm. First, the soil was evenly distributed in the cell

Table 2
Anion and cation composition of saturation extract from Grout Vault Soil (meq/l-extract)[a]

SO_4^{-2}	Na^+	T-Alk[b]	Ca^{+2}	NO_3^-	K^+	Mg^{+2}	Cl^-
0.62	1.09	2.70	0.89	0.11	0.12	0.36	0.05

[a]Only species with concentrations ≥ 0.05 meq/l are listed. Adapted from reference [15].
[b]Total Alkalinity (T-Alk) is reported as carbonate, CO_3^{-2}.

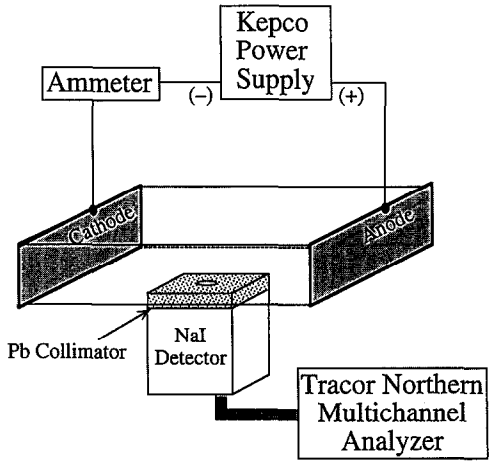

Fig. 1. Schematic diagram of the electrochemical cell and instrumentation used to make real-time spatially-resolved measurements of $^{137}Cs^{+}$ radiotracer transport during the passage of current through saturated Hanford Grout Vault Soil.

and then packed with a five pound brick to minimize void space. After the soil was packed, a small volume ($\approx$ 5 ml) was removed from the midpoint of the cell and it was replaced with saturated soil containing a 20 μCi 'spike' of $^{137}Cs^{+}$ and 0.5 M $^{133}CsNO_3$. The cell sat on a 0.95 cm thick aluminum plate above a NaI scintillation counter with a 5.08 cm thick lead collimator having a 0.95 cm diameter aperture. The aluminum plate served as a support so the cell could be manually moved to selected positions over the aperture in the lead collimator, thus providing spatially-resolved radiotracer measurements. The cell was positioned as close as possible to the detector to minimize radioactive decay due to detector-source separation.

A Tracor Northern (Model TN-2700) multichannel analyzer was used to read the gamma radiation spectrum from the NaI detector. The analyzer used an auxiliary high voltage supply to power the NaI detector. The detector efficiency was optimized for ^{137}Cs gamma rays at 662 keV, and good counting statistics were obtained with an integration time of 180 seconds. The detector operating voltage was +1080 V. The ^{137}Cs radioactivity was calculated as the integrated counts under the 662 keV ^{137}Cs emission line in the energy spectrum divided by the integration time. Electrochemical transport in the cell was controlled using a Kepco (Model HB8A) power supply that set a constant 200 V bias between the two electrodes. Current was measured using an HP (Model 3438A) multimeter.

Once the cell was prepared with a radioactive GSV sample, it was allowed to sit for 24 h with no applied potential in order to assess the significance of diffusion in the system. After the initial 24 h period, the potential was applied and the motion of the radioactive cesium 'spike' was monitored approximately every 24 h for nine days. After the experiment was terminated, the role of electroosmotic convection was assessed by measuring the moisture content of the soil at numerous positions along the length of the cell.

2.3. Conductivity measurements

A schematic of the cylindrical soil column (4.1 cm diameter × 15.9 cm length), the platinum anode and cathode, the palladium reference electrodes, and instrumentation is show in Fig. 2. The anode and cathode were 0.1 mm diameter platinum mesh electrodes that were held in place by an assembly consisting of two plastic O-rings, a solid Teflon disk, and a rubber O-ring. The cell endcaps were sealed to limit flow in and out of the soil column. Before each experiment, the GVS was soaked for a minimum of two weeks in an excess of 1.5 mM Na_2SO_4 solution (preliminary experiments showed that a two week pre-equilibration period was needed to obtain a stable conductivity reading from the soil when no current was passed). The soil cylinder was then filled with saturated GVS by fixing one platinum electrode endcap assembly and slowly adding soil to the cylinder, taking care to pack the soil tightly as filling progressed. As the cylinder was filled to the level of each interior reference electrode, the electrode was inserted into the soil before adding more soil. The reference electrode ports were sealed to avoid the loss of electrolyte during the packing procedure. Once the soil cylinder was filled and capped with the second platinum mesh electrode assembly, the column was connected to the instrumentation.

The cathode and anode were connected to the working and counter electrode contacts, respectively, of the Princeton Applied Research (Model 273A) Potentiostat/Galvanostat. The four interior reference electrodes (labeled Ref 1–4) were connected to a computer controlled electronic relay switch, as was the anode. The electronic relay switch allowed the potentiostat/galvanostat to measure the potential of the cathode relative to that of the four interior electrodes and the anode. The potentiostat/galvanostat was interfaced to an Apple computer (Macintosh Centris 650) via GPIB, and the particular reference electrode was selected by the electronic relay switch

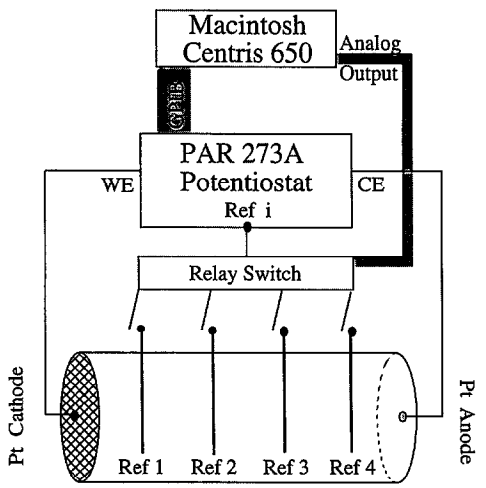

Fig. 2. Schematic diagram of the electrochemical cell and instrumentation used to make real-time spatially-resolved measurements of soil conductivity during the passage of current through Hanford Grout Vault Soil.

via an analog signal. All experiments were run under galvanostatic conditions with current levels between 0.06 mA and 0.60 mA.

Once the system was filled with GVS and the instrumentation was prepared, the soil conductivity was checked to ensure it remained stable when there was no sustained current applied to the system. After 4–12 h of checking the stability of the conductivity, the current was turned on for the duration of the experiment. For the first 12 h, the conductivity was measured at each electrode location once every ten minutes using the current interruption method (described in the next section). After that, the conductivity measurements were made hourly. Each experiment lasted between 58 and 626 h, depending on the current level applied.

3. Results and discussion

In Fig. 3(a), the integrated intensity of the 662 keV $^{137}Cs^+$ emission line is shown as a function of spatial location when there is a 20 μCi $^{137}Cs^+$ 'spike' placed in the center of the cell at a distance of 11.43 cm from the anode. The open circles in Fig. 3(a) correspond to signal acquired 24 h before a bias voltage was applied to the cell and the open squares correspond to signal acquired right at the moment when bias was applied. It is clear from the data that the diffusion of Cs^+ is not significant over the one day period considered. Thus, transport by diffusion is a slow process in this system, as it is in most soils [17].

Another feature displayed by Fig. 3(a) is a significant level of instrumental broadening that reduces the spatial resolution of the method. Since the actual $^{137}Cs^+$ concentration is a 'spike' of essentially zero spatial width (a Dirac delta function), it is easily shown (with the aid of the deconvolution theorem) that the spatial profile of the measured signal in Fig. 3(a) is identical to the instrumental response function. Thus, the fast Fourier transform (FFT) of the instrumental response, represented by Fig. 3(a), can be deconvoluted from all of the spatially resolved measurements to give a more accurate picture of the true $^{137}Cs^+$ concentration profile. Mathematically, this deconvolution operation is represented by

$$c(x) = \Im^{-1}\{\Im\{s(x)\}/\Im\{r(x)\}\}, \tag{1}$$

where $c(x)$ is the true $^{137}Cs^+$ concentration profile, $\Im\{s(x)\}$ is the FFT of the measured signal, and $\Im\{r(x)\}$ is the FFT of the instrumental response to an infinitesimally thin spike of $^{137}Cs^+$.

Fig. 3(b) shows the real-time evolution of the deconvoluted $^{137}Cs^+$ concentration profile when a 200 V bias is applied at time zero. The concentration profile begins as a 20 μCi spike centered 11.43 cm from the anode. As time evolves, the $^{137}Cs^+$ spike moves steadily toward the cathode and broadens. The $^{137}Cs^+$ concentration profile displays a fairly sharp leading front as it moves, but the trailing edge of the evolving profile becomes increasingly extended as time progresses. For example, consider the $^{137}Cs^+$ concentration at the center of the cell (11.43 cm) where the original spike was placed. In 53 h, the initial 20 μCi of $^{137}Cs^+$ is reduced by 75% to approximately 5 μCi. After 69 more hours of applied bias, the 5 μCi is again reduced by roughly 75% to 1.4

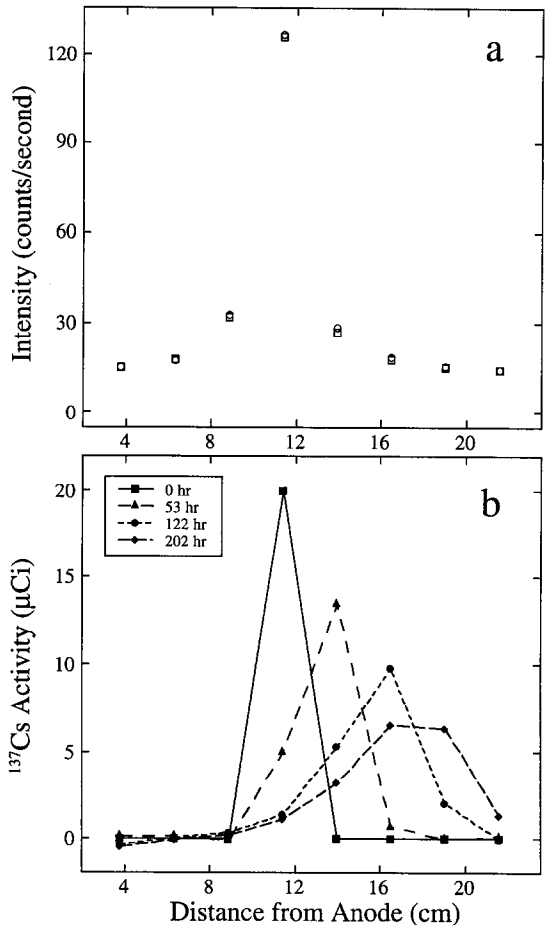

Fig. 3. Real-time spatially resolved radiotracer measurements. (a) Spatially-resolved signal intensity from a 20 μCi 'spike' of $^{137}Cs^+$ that is located in the center of the cell (11.43 cm from the anode). The system was allowed to sit static to see if significant diffusion occurred in 24 h (open circles: initial 'spike'; open squares: after 24 h). (b) The time evolution of the $^{137}Cs^+$ profile upon application of 200 VDC applied bias. Time steps are shown after 0 h (■), 53 h (▲), 122 h (●), and 202 h (◆) of applied bias.

μCi. However, as time progresses further, the remaining $^{137}Cs^+$ is increasingly difficult to remove; in 80 more hours the $^{137}Cs^+$ concentration is reduced by a mere 21% to 1.1 μCi of residual signal. One can see from the data in Fig. 3(b) that nearly 95% of the initial Cs^+ spike has been removed from the center of the cell, but remediating the remaining 5% becomes increasingly difficult with time. The long trailing edge of the moving front, and the difficulty in removing residual $^{137}Cs^+$, suggests that cesium is probably bound to Hanford sediments. Strong binding of cesium has been noted before and has prompted the need for further study of sequestering agents for Cs desorption from Hanford soil [18]. No appreciable change in overall moisture content, or its spatial distribution, was measured in these closed-cell experiments.

The results in Fig. 3(b) show that radiotracer measurements provide real-time, spatially-resolved monitoring of a target species in a laboratory-scale experiment. Having a tool capable of resolving the profile of a single species, in real-time, should allow for future advances in process optimization and control. However, radiotracer methods such as this cannot be easily applied in the field, and they do not provide information about the chemical form of the species or its local chemical environment. Carefully executed soil conductivity measurements can provide complementary information to radiotracer techniques, and conductivity can easily be measured in the field with good temporal and spatial resolution.

Soil conductivity measurements are of great value, especially when coupled with thorough geochemical and geophysical data, because the conductivity of soil (or any charged porous medium) depends on the surface charge of the medium, the ionic strength of the pore fluids, and geometric factors associated with the porous network. The relationship between surface charge, electrolyte composition, and conductivity of a porous medium can be explored by considering the average conductivity of a single cylindrical pore of radius r with a surface charge q_s [19]

$$\kappa_{ave} = \kappa^0 \left\{ 1 + \frac{q_s \lambda F}{\varepsilon RT} \left(\frac{2\lambda}{r} - \frac{1}{I_1} \right) \frac{\sum_i z_i^3 u_i c_i^0}{\sum_i z_i^2 u_i c_i^0} \right\}, \tag{2}$$

where $\kappa^0 = F^2 \sum_i z_i^2 u_i c_i^0$ is the conductivity at the centerline of the pore, λ is the Debye length, ε is the dielectric constant of the medium, I_1 is the modified Bessel function of the first kind of order one (evaluated at r/λ), and z_i, u_i and c_i^0 are, respectively, the charge, mobility, and centerline concentrations of species i in the pore. Eq. (2) includes contributions from current carried via electrolyte in the core of the pore and from current flowing through the electrical double layer. From Eq. (2), it is clear that the average conductivity of a charged pore can be greater than or less than the conductivity of an uncharged pore, depending on the sign of the surface charge and the sign of the summation terms where the ionic properties of the electrolyte are taken into account. Thus, the macroscopic conductivity of a porous medium is controlled by physical properties that affect the conductivity of the individual pores (e.g. surface charge, species mobilities, concentration, etc.), in addition to the well-known contribution of the porous network's geometric factors (e.g. tortuosity and degree of saturation).

Proper experimental measurements of conductivity require the use of dynamic electrochemical methods — either high frequency AC impedance [20] or current interruption [21] — rather than simple DC measurements. The principle behind dynamic conductivity measurements is that the time-scale for establishing a migration flux is much faster than any other time-scale in an electrochemical system. High frequency AC impedance and current interruption methods are routine in-situ electrochemical measurements that form the basis of all commercial conductivity meters. Current interruption is a turn-key feature of the potentiostat used for these experiments. The fact that DC conductivity measurements always yield a conductivity that is lower than the true conductivity of the medium has been recognized for some time in the electrochemical remediation literature [4]. However, to the best of our knowledge, all past experiments reported in the literature have measured conductivity as a post-remediation diagnostic, rather than as a real-time spatially-resolved measurement.

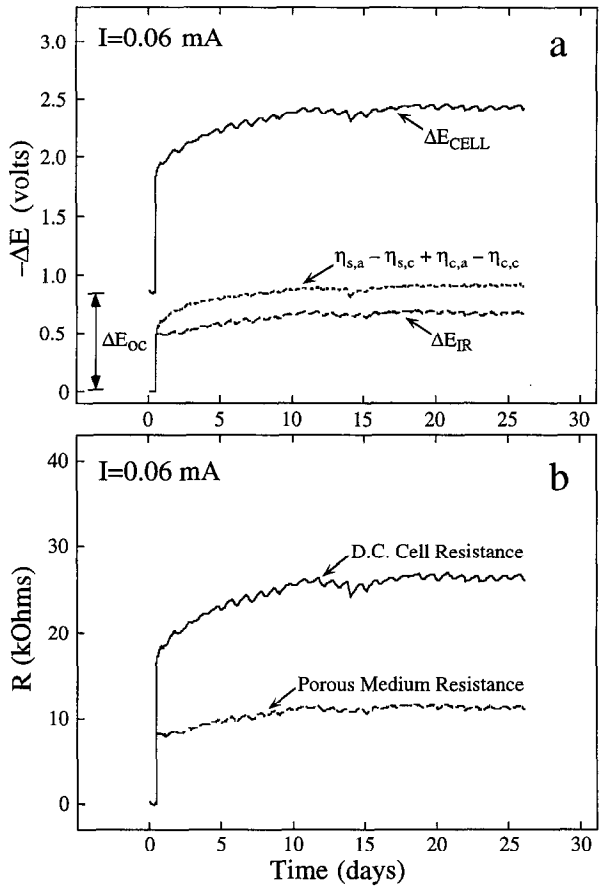

Fig. 4. Cell potential measurements and their impact on measured resistance of the medium. (a) The time evolution of overall cell potential (ΔE_{CELL}) and its component potentials — the ohmic drop through the medium (ΔE_{IR}), the electrode overpotentials ($\eta_{s,a} - \eta_{s,c} + \eta_{c,a} - \eta_{c,c}$), and the open circuit potential (ΔE_{OC}) — are shown for an applied current of 0.06 mA. (b) The time evolution of the D.C. cell resistance (calculated from $\{\Delta E_{CELL} - \Delta E_{OC}\}/I$) is compared to the actual porous medium resistance ($\Delta E_{IR}/I$).

Fig. 4 illustrates experimental conditions where DC measurements give a resistance that is more than twice the true resistance of the medium to ion conduction. Fig. 4(a) shows the total applied bias to the cell ($\Delta E_{CELL} - \Delta E_{OC}$) measured during the passage of a steady 0.06 mA of current. From the data in Fig. 4(a) (obtained using the current interruption function on the potentiostat), one finds for this low current level that the applied cell bias is composed predominantly of the surface and concentration overpotentials at the anode and cathode (denoted $\eta_{s,a} - \eta_{s,c} + \eta_{c,a} - \eta_{c,c}$). The ohmic potential drop through the ion conducting medium is only 40% of the total applied bias. If the DC cell resistance (or 'apparent' resistance [4]) is defined as the applied bias divided by the current, $(\Delta E_{CELL} - \Delta E_{OC})/I$, then one overestimates the actual porous medium resistance ($\Delta E_{IR}/I$) by roughly 250%, as shown in Fig. 4(b). It is also worthwhile noting

that poor contact between the saturated soil and the electrode should be easily diagnosed by separating the applied bias into the electrode overpotentials and porous medium ohmic drop. In particular, one would see a significant increase in the electrode overpotential contribution if the active area of the electrode contacting the electrolyte declined (high local current densities require high overpotential driving forces, even if the area-averaged current density remains constant). Fig. 4 displays a well-behaved overpotential contribution during the 26 day experiment, suggesting that good contact between the soil and electrode is maintained. Though the example shown in Fig. 4 is made dramatic by the use of a modest current, one can normally assume there will be a few volts of electrochemical overpotential contribution under typical experimental conditions. Thus, electrochemical overpotential contributions may significantly affect DC measurements whenever the measured DC potential is under roughly 50 V.

The conductivity of a particular region in the cell is found by making sequential current interruption measurements between different pairs of electrodes. If the cathode is denoted by the subscript c and each of the other electrodes by the subscript $i = 1, \ldots, 5$, where 5 is the anode, then current interruption using electrode i as the reference provides $R_{i,c}$, the porous media resistance between the cathode and the reference i. Since the resistance of each section of the porous medium has series additivity, the local resistance of the medium between any two points, say, reference electrodes 3 and 4, is simply given by $R_{3,4} = R_{4,c} - R_{3,c}$, or more generally, $R_{i,j} = R_{j,c} - R_{i,c}$. Once the local resistance is known, the local conductivity (for this cell geometry) is given by

$$\kappa_{i,j} = \frac{l_{ij}}{R_{ij}A}, \tag{3}$$

where l_{ij} is the distance between electrodes i and j, and A is the cross sectional area of the cell.

Fig. 5 shows typical behavior for the local evolution of soil conductivity as a function of time (bottom axis) and milliequivalents of charge (top axis). Conductivity is plotted in Fig. 5 as the fractional change in conductivity

$$\Delta\kappa/\kappa_0 = \frac{\kappa(t) - \kappa(0)}{\kappa(0)}, \tag{4}$$

for each region of the cell (the regions are shown in the cell configuration schematic at the top of the figure). For example, the $\Delta\kappa/\kappa_0$ data in Fig. 5 with the symbol (●) shows the fractional change in $\kappa_{2,1}$ with time. The milliequivalents of charge passed, It/F, is equivalent to the number of millimoles of OH^- added at the cathode via the water electrolysis reaction

$$2H_2O + 2e^- \rightarrow H_2 + 2OH^- \tag{5}$$

and H^+ added at the anode via the water electrolysis reaction

$$2H_2O \rightarrow O_2 + 4H^+ + 4e^-, \tag{6}$$

provided there is perfect faradaic efficiency for the electrolysis reactions.

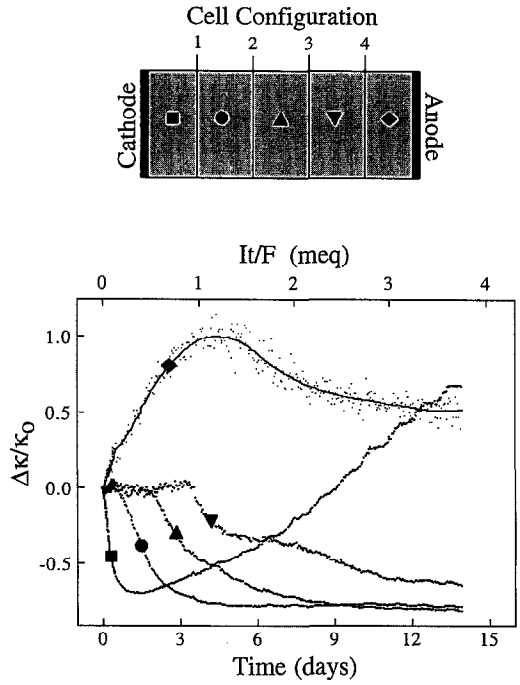

Fig. 5. Real-time spatially-resolved conductivity measurements. The fractional change in conductivity ($\Delta\kappa/\kappa_o$) for each spatial section of the cell is plotted as a function of time for an applied current of 0.30 mA. Each data curve has a symbol that corresponds to a spatial location shown in the cell configuration schematic.

Fig. 5 shows that immediately upon passage of current, the conductivity in the vicinity of the cathode drops precipitously and the conductivity in the vicinity of the anode rises. Throughout the remainder of the cell the conductivity is essentially constant. After about one day, a sharp decrease in conductivity is observed in region 2,1 (●), and this declining conductivity appears to propagate as a sharp front away from the cathode and into region 3,2 (after roughly 2.5 days), then into region 4,3 (after roughly 4 days), and finally into the region adjacent to the anode (after roughly 5.5 days). Conversely, the increasing conductivity appears to propagate away from the anode region much more slowly; e.g., a small positive deviation in conductivity (a 'hump') begins to show up in region 4,3 (▼) after about 5 days. Thus, the decreasing conductivity front generated by the cathode moves roughly 5 times faster than the increasing conductivity front generated by the anode.

Since electromigration is normally the predominant mode of transport when current is passed through soil [17], it is reasonable to assume that the cathode-generated conductivity front is caused by an ionic species (or multiple species with nearly equal mobilities) moving via electromigration alone. If this is the case, then the distance the front moves in time t should be given by

$$X_{\text{front}} = \left(\frac{F^2 u_i}{\kappa}\right)\left(\frac{It}{F}\right), \tag{7}$$

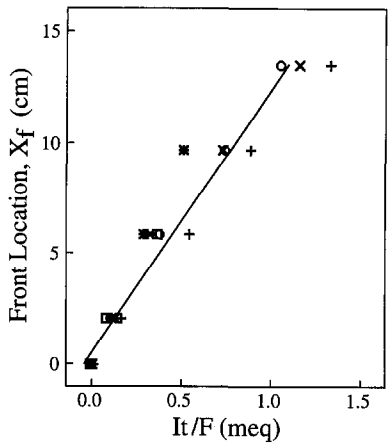

Fig. 6. The spatial location of the conductivity front generated by the cathode (X_f) is shown as a function of the millequivalents of charge added to the system (It/F) for five different applied currents (0.06 mA $\leq I \leq$ 0.6 mA).

assuming the medium has constant conductivity. Eq. (7) shows that experiments performed at different currents should collapse to one straight line if the location of the front, X_{front}, is plotted as a function of the charge passed, It/F. Fig. 6 shows that the location of the negative-going front tends toward a single fairly straight line for all of our experimental runs. Observed deviations from a single line can be attributed to the fact that conductivity is not constant in these experiments and there are also some differences in the magnitude of κ between runs (due mainly to the reproducibility of packing soil in the cell).

Eq. (7) also shows that the velocity of a conductivity front is proportional to the ionic mobility of the one (or many) species responsible for the front formation. At first pass, it seems probable that the decreasing conductivity front generated by the cathode results from hydroxide liberated during water reduction, Eq. (5), and the increasing conductivity generated by the anode results from protons liberated during water oxidation, Eq. (6). However, the anode-generated front moves much slower than the cathode-generated front, so it is highly unlikely that protons — ions with extremely high mobilities — are the predominant species carrying the current in the anode generated front. Rather, it seems more likely that protons generated at the anode react with a soil constituent such as a precipitated carbonate (GVS is alkaline and naturally contains calcium carbonate, see Tables 1 and 2) to form less mobile free ions, e.g.,

$$CaCO_3 + H^+ \rightarrow Ca^{+2} + HCO_3^- . \tag{8}$$

The reaction given by Eq. (8) accounts for both the sharp rise in conductivity near the anode (more free charge carriers are added to the medium) and the slow propagation of the front (the mobilities of Ca^{+2} and HCO_3^- are roughly a fifth that of OH^- and a tenth that of H^+).

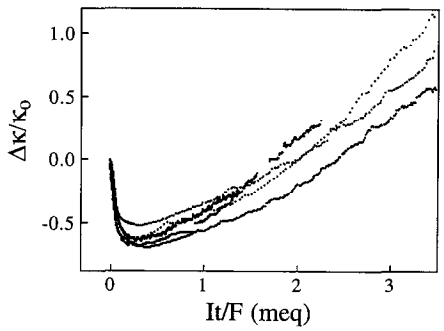

Fig. 7. The evolution of conductivity in the vicinity of the cathode (denoted by ■ in Fig. 5) as a function of milliequivalents of charge added for five different applied currents (0.06 mA $\leq I \leq$ 0.6 mA).

A question worth exploring in greater detail is the physicochemical origin of decreasing conductivity in soil subjected to cathode-generated hydroxides. Recall from Eq. (2) that the conductivity of a pore — the most basic element of a porous medium — decreases if the free ion concentration decreases or the negative surface charge on the soil increases (assuming no changes to the porous medium's geometric factors). From the arguments made above regarding the velocity of the front, it appears clear that OH^- is the species carrying most of the current between the cathode and the leading edge of the front. Plotted in Fig. 7 is the conductivity change in the region next to the cathode (denoted by ■ in Fig. 5) as a function of the charge passed during each of our experimental runs. Two features of Fig. 7 stand out. First, all of the curves reach a minimum conductivity after about 0.3 meq of OH^- have been added at the cathode, independent of the electromigration rate (for 0.06 mA $\leq I \leq$ 0.6 mA). Second, after reaching their minimum conductivity, all of the curves exhibit a significant recovery where the conductivity can actually exceed the initial values. The first observation suggests that either a fixed number of surface sites are being titrated by the added hydroxide via a reaction such as [22]

$$\equiv Si\text{–}O\text{–}H + OH^- \rightarrow \equiv Si\text{–}O^- + H_2O, \tag{9}$$

or a fixed amount of hydroxide precipitate forms. The second observation suggests that a pore-plugging precipitate does not in fact form, since the conductivity would not be likely to recover to the extent it does if the initial drop in conductivity was mainly from an obstruction of the porous structure. Thus, it seems probable that hydroxide produced by water reduction leads to the titration of surface groups and an increase in the negative surface charge. In fact, a common method for measuring surface charge in colloidal systems is to titrate the surface with a base while monitoring the conductivity [23]. The method, called conductometric titration, yields curves that look remarkably like Fig. 7. The minimum conductivity is reached when all the surface groups have been titrated to there anionic form; further addition of base simply adds free ions to solution causing the conductivity to increase.

One final word is in order regarding Fig. 7. The fact that all of the curves overlay in Fig. 7 indicates that chemical rates are much faster in this system than are the transport rates, at least for the range of currents studied. In other words, chemical reversibility

holds for these experiments. The assumption of chemical reversibility is central to most models of transport and reaction in soil [7,10,13,14]. Fig. 7 shows that carefully executed conductivity measurements can be used to ensure the validity of that assumption.

4. Concluding remarks

A tremendous amount of information can be gleaned about the fate of contaminants and the interaction of electrolysis products with soil by using simple real-time spatially-resolved monitoring techniques that are combined with thorough geochemical and geophysical data sets. Radiotracer techniques allow the extent that a radioactive species is remediated to be unambiguously determined in the laboratory, and the method also provides insight into the immobilization of Cs^+ by adsorption to the soil. Radiotracer methods are especially well-suited for evaluating process feasibility and optimization issues in the laboratory. Conductivity measurements, on the other hand, cannot provide detailed information about the fate of a specific contaminant. Instead, real-time and spatially-resolved conductivity measurements provide a window into the changing state of the porous medium and the propagation of electrochemically-generated species that are introduced by the passage of current. Conductivity measurements are readily performed in either the laboratory or the field. Despite the attributes of the techniques described here, inexpensive sensors that have the specificity of radiotracer techniques and the robustness of conductivity measurements are needed to improve the effectiveness and reduce the cost of field-scale in-situ remediation technologies.

Acknowledgements

This work was supported in part by a Department of Energy Junior Faculty Award in Environmental Restoration and Waste Management, administered by Oak Ridge Associated Universities under management and contract DE-AC05-76OR0003, and by a U.W. Royalty Research Fund award. Pacific Northwest Laboratory is operated for the U.S. Department of Energy by Battelle Memorial Institute under contract DE-AC06-76RLO1830.

References

[1] S. Banerjee, J. Horng, J.F. Ferguson, P.O. Nelson, Field-scale feasibility of electrokinetic remediation, Report Presented to USEPA, Land Pollution Control Division, RREL, CR811762-01 (1990).

[2] D.D. Runnells, C.G. Patterson, Electromigration as a method for in-situ remediation of sulfate and other highly soluble contaminants in ground water, in: F.G. Will (Ed.), Proc. of EPRI Workshop on In-situ Electrochemical Soil and Water Remediation, Electric Power Research Institute Publication No. TR-104170 (Palo Alto, CA, 1994) pp. 85–114.

[3] R. Lageman, Electroreclamation: Applications in The Netherlands, Environ. Sci. Tech. 27 (1993) 2648–2650.

[4] J. Hamed, Y.B. Acar, R.J. Gale, Pb(II) removal from kaolinite by electrokinetics, J. Geotech. Eng. 117 (1991) 241–271.
[5] Y.B. Acar, J.T. Hamed, A.N. Alshawabkeh, R.J. Gale, Removal of cadmium(II) from saturated kaolinite by the application of electrical current, Geotechnique 44 (1994) 239–254.
[6] A. Ugaz, S. Puppala, R.J. Gale, Y.B. Acar, Electrokinetic soil processing: Complicating features of electrokinetic remediation of soils and slurries: Saturation effects and the role of the cathode electrolysis, Chem. Eng. Comm. 129 (1994) 183–200.
[7] Y.B. Acar, R.J. Gale, A.N. Alshawabkeh, R.E. Marks, S. Puppala, M. Bricka, R. Parker, Electrokinetic remediation: Basics and technology status, J. Haz. Mat. 40 (1995) 117–137.
[8] S. Pamukcu, J.K. Wittle, Electrokinetic removal of selected heavy metals from soil, Environ. Prog. 11 (1992) 241–250.
[9] J.B. Jensen, V. Kubes, M. Kubal, Electrokinetic remediation of soils polluted with heavy metals. Removal of zinc and copper using a new concept, Environ. Tech. 15 (1994) 1077–1082.
[10] A.P. Shapiro, P.C. Renaud, R.F. Probstein, Preliminary studies on the removal of chemical species from saturated porous media by electroosmosis, Physicochem. Hydrodynamics 11 (1989) 785–802.
[11] A.P. Shapiro, R.F. Probstein, Removal of contaminants from saturated clay by electroosmosis, Environ. Sci. Tech. 27 (1993) 283–291.
[12] R.F. Probstein, R.E. Hicks, Removal of contaminants from soils by electric fields, Science 260 (1993) 498–503.
[13] R.E. Hicks, S. Tondorf, Electrorestoration of metal contaminated soils, Environ. Sci. Tech. 28 (1994) 2203–2210.
[14] R.A. Jacobs, M.Z. Sengun, R.E. Hicks, R.F. Probstein, Model and experiments on soil remediation by electric fields, J. Environ. Sci. Health A29 (1994) 1933–1955.
[15] R.J. Serne, J.L. Conca, V.L. LeGore, K.J. Cantrell, C.W. Lindenmeier, J.A. Campbell, J.E. Amonette, M.I. Wood, Solid Waste Leach Characteristics and Contaminant-Sediment Interactions: Batch Leach and Adsorption Tests and Sediment Characterization, Vol. 1, Pacific Northwest Laboratory, PNL-UC-512 Richland, Washington (1993).
[16] J. Virden, J. Surma, M. Buehler, S. Mattigod, D. Lessor, L. Peurrung, G. Pillay, P. Gauglitz, Electrokinetic Remediation of Hanford Soil, Pacific Northwest Laboratory, PNL-9389 Richland, Washington (1993).
[17] Y.B. Acar, A.N. Alshawabkeh, Principles of electrokinetic remediation, Environ. Sci. Tech. 27 (1993) 2638–4267.
[18] M.F. Buehler, J.E Surma, J.W. Virden, In situ soil remediation using electrokinetics, in: G.W. Gee and N.R. Wing (Eds.), In-situ Remediation: Scientific Basis for Current and Future Technologies, Vol. 2 (Battelle Press, 1995) pp. 991–1010.
[19] J. Newman, Electrochemical Systems (Prentice-Hall, Englewood Cliffs, NJ, 1973) pp. 190–201.
[20] A.J. Bard, L.R. Faulkner, Electrochemical Methods (John Wiley and Son, New York, 1980) pp. 345–353.
[21] E. Yeager, J. Kuta, Techniques for the study of electrode processes, in: H. Eyring (Ed.), Physical Chemistry, An Advanced Treatise, Vol. IXA (Academic Press, New York, 1970) pp. 345–461.
[22] L.K. Koopal, Adsorption of Ions and Surfactants, Surfactant Science Series: Coagulation and Flocculation, Vol. 47 (Marcel Dekker, New York, 1993) pp. 101–208.
[23] L. Meites, H.C. Thomas, Advanced Analytical Chemistry (McGraw-Hill, New York, 1958).